chemosensors

MDPI

Article

Enhanced Electrochemical Glucose Sensing via AuNP-Assisted Electrodeposition and Yeast Modification

Teresė Kondrotaitė-Intė [1], Domas Pirštelis [2], Laisvidas Striška [3], Antanas Zinovičius [4,5], Inga Morkvėnaitė [3,*] and Arūnas Ramanavičius [2,*]

[1] Department of Mechanical and Materials Engineering, Vilnius Gediminas Technical University, LT-10105 Vilnius, Lithuania; terese.kondrotaite-inte@vilniustech.lt
[2] Department of Physical Chemistry, Faculty of Chemistry and Geosciences, Vilnius University, Naugarduko St. 24, LT-03225 Vilnius, Lithuania; domas.pirstelis@ftmc.lt
[3] Department of Electrical Engineering, Vilnius Gediminas Technical University, Plytines St. 25, LT-10105 Vilnius, Lithuania; laisvidas.striska@ftmc.lt
[4] Department of Mechatronics, Robotics, and Digital Manufacturing, Vilnius Gediminas Technical University, Plytines St. 25, LT-10105 Vilnius, Lithuania; antanas.zinovicius@vilniustech.lt
[5] Department of Nanotechnology, State Research Institute Centre for Physical Sciences and Technology (FTMC), Sauletekio av. 3, LT-10257 Vilnius, Lithuania
* Correspondence: i.morkvenaite@vilniustech.lt (I.M.); arunas.ramanavicius@chf.vu.lt (A.R.)

Abstract

This study investigates the combined effect of electrodeposited gold nanoparticles (AuNPs) and AuNP–polypyrrole (PPy)-modified Saccharomyces cerevisiae on electrochemical glucose sensing. AuNPs were deposited onto electrode surfaces by cyclic voltammetry, and the resulting interfaces were characterized using atomic force microscopy, cyclic voltammetry, and electrochemical impedance spectroscopy. AFM analysis confirmed increased surface roughness and height variability after deposition, indicating substantial restructuring of the electrode interface. Electrochemical measurements showed that AuNP deposition altered interfacial charge storage and transfer and increased the measured charge-transfer resistance. Glucose sensing was evaluated in a ferricyanide-mediated system using yeast layers with or without AuNP and PPy modification over a 0–60 mM concentration range. All configurations exhibited saturating, non-linear glucose responses described by Hill fitting. Among the evaluated yeast-modified electrodes, the AuNP–PPy modified yeast produced the strongest glucose-induced current increase and the best low-concentration performance, achieving a limit of detection of 0.540 mM, compared with 1.016 mM and 1.330 mM for single-modified layers and 3.360 mM for unmodified yeast. These results show that combining AuNP electrodeposition with AuNP–PPy yeast modification improves interfacial properties and enhances mediator-assisted electrochemical glucose sensing.

Keywords: biosensors; gold nanoparticles; polypyrrole; electrodeposition

Check for updates

Received: 31 December 2025
Revised: 25 February 2026
Accepted: 26 February 2026
Published: 12 March 2026

Copyright: © 2026 by the authors. Licensee MDPI, Basel, Switzerland. This article is an open access article distributed under the terms and conditions of the Creative Commons Attribution (CC BY) license.

1. Introduction

Electrochemical biosensing is fundamental to analytical platforms for clinical diagnostics [1], food quality control [2], and bioprocess monitoring [3], where the rapid and reproducible quantification of essential metabolites, such as glucose, is necessary. A bioelectrochemical system (BES) facilitates the conversion of chemical energy to electrical energy or the reverse by integrating biological and electrochemical processes. This capability enables their use in biosensing [4] and other applications, such as wastewater treatment [5], biohydrogen production [6], and the operation of small-scale point-of-care devices [7].

Among these, microbial fuel cells (MFCs) have garnered considerable interest as bioelectrochemical devices that produce electricity via microbial metabolism [8,9]. MFCs can be modified for sensing applications, utilizing the metabolic activity of microorganisms as the transduction mechanism for chemical detection. In MFC-based sensors, target analytes influence microbial oxidation processes, resulting in quantifiable alterations in the electrical output that can be associated with analyte concentration. In glucose-responsive MFC configurations, the uptake and metabolism of glucose by microbes facilitate the release of electrons and the generation of current, which allows for the quantification of glucose through the resulting electrochemical signal [10,11]. In this context, whole-cell systems and microbial bioelectrodes offer strong biocatalytic functionality; however, their analytical performance is often constrained by inefficient charge transfer at the bio–electrode interface and by weak or unstable cell attachment on traditional electrode surfaces [12,13].

MFC consists of anodic and cathodic chambers that are separated by a proton exchange membrane or a salt bridge [14]. In a standard microbial fuel cell, electroactive bacteria located on the anode oxidize substrates, resulting in the release of electrons and protons. The electrons move through an external circuit to arrive at the cathode, where they engage in a reduction reaction, typically the oxygen reduction reaction, and thereby generate the electricity [15,16]. The anode functions as the primary interface for microorganism adhesion and electron transfer, making its material properties play a crucial role in influencing the magnitude, stability, and reproducibility of the sensing signal in MFC-based biosensors [17]. An effective anode material should demonstrate several essential characteristics, such as high electrical conductivity with low resistance, good biocompatibility, robust chemical and corrosion stability, a large specific surface area, and adequate mechanical strength and durability [18]. In recent years, various materials have been investigated for anode fabrication in microbial fuel cells, particularly carbon-based materials, metallic substrates, and electrically conducting polymers [11,19–21]. Among these options, carbon-based materials have garnered significant attention and are most frequently utilized as anodes in microbial fuel cells [22]. Gold nanoparticles (AuNPs) are utilized in the modification of anodes to enhance electrode roughness and surface area accessibility, improve electrical contact and conductivity at the microbe–electrode interface, adjust surface chemistry for biofilm attachment, and offer well-dispersed catalytic sites that are compatible with biofilms [21,23–25]. The existing experimental literature that specifically quantifies standalone AuNP-only anodes is scarce; the majority of published studies incorporate AuNPs within composites (such as PANI/AuNP, AuNPs supported on graphene/CNT, or biogenic AuNPs) [24,26–28]. In the majority of documented investigations, gold nanoparticles are produced through chemical methods that utilize hazardous reagents and harsh reaction conditions [29,30]. The application of pre-synthesized citrate-stabilized AuNPs, as used in this study, facilitates precise and consistent anode modification, eliminating the necessity for in situ synthesis. This approach reduces direct exposure to hazardous materials while maintaining the integrity of nanoparticle size, dispersion, and surface properties. This study utilizes 10 nm gold nanoparticles (AuNPs) due to their established balance of high specific surface area, colloidal stability, and effective electron transfer performance in bioelectrochemical systems. Earlier investigations have shown that AuNPs around 10 nm in size display advantageous biocompatibility and efficient interactions with microbial cell surfaces and redox-active proteins [31]. The choice of size is reinforced by findings suggesting that ultrasmall nanoparticles (<5 nm) can lead to heightened cytotoxic effects, while larger nanoparticles typically show decreased surface reactivity and lower electron transfer efficiency because of a smaller surface-to-volume ratio [32–34].

In the last twenty years, numerous microorganisms have been explored for their potential in bioelectrochemical applications [35]. This includes various representa-

tives from *Acidobacteria*, *Actinobacteria* [36], α-*Proteobacteria* [37], β-*Proteobacteria* [38], γ-*Proteobacteria* [39], δ-*Proteobacteria* [40], and ε-*Proteobacteria* [41], alongside *Firmicutes* [42], yeast [11,43–45], and algae [46]. Multiple strains of yeast have been examined for their electrogenic properties [47,48]. Among these microorganisms, *Saccharomyces cerevisiae* has been widely used in fungi-based bioelectrochemical platforms because of its accessibility, straightforward cultivation process, and operational ease, which eliminates the stringent anaerobic conditions and handling difficulties often linked with numerous electroactive bacterial systems [49]. Thus, *S. cerevisiae* provides an effective and scalable biocatalyst for the development and systematic assessment of nanostructured carbon bioelectrodes aimed at mediator-assisted electrochemical glucose response.

In this work, glucose is transduced through mediator-assisted electron harvesting from yeast metabolism, rather than by direct glucose oxidation at graphite. Following glucose uptake stimulates yeast metabolism, increasing availability of intracellular electron carriers such as NADH [50], which can be transferred directly or via cellular redox sites to an external mediator system (potassium ferricyanide and the immobilized quinone mediator). The mediator is then re-oxidized at the electrode, producing an increased anodic current [51]. While glucose oxidase-based electrodes offer high specificity, their performance depends on enzyme immobilization and long-term enzyme stability and may involve oxygen/peroxide chemistry depending on design [52,53]. In contrast, whole-cell sensing layers can be robust, low-cost, and self-regenerating, supporting applications such as bioprocess/fermentation monitoring and proof-of-concept bioelectrode engineering focused on interfacial charge transfer [54,55].

This study aims to determine how electrochemically deposited AuNPs and yeast surface functionalization influence the glucose-responsive electrochemical performance of graphite-based *S. cerevisiae* bioelectrodes.

2. Materials and Methods

2.1. Materials

YPD broth, pyrrole (98%), poly-L-lysine, 9,10-phenanthrenequinone (PQ), and D-(+)-glucose (99%) were purchased from Merck (Carrigtohill, Ireland). Baker's yeast (commercial grade) was purchased from the food supplier Dr. Oetker Lietuva (Vilnius, Lithuania). Ethanol (97%) was purchased from UAB Vilniaus Degtinė (Vilnius, Lithuania). Sigma–Aldrich (Steinheim, Germany) was the source of Whatman® Nuclepore track-etched membranes, graphite electrodes, and all other chemicals unless stated otherwise.

PBS (pH 6.8) was prepared in distilled water by combining sodium acetate (CH_3COONa, 0.05 M), disodium phosphate (Na_2HPO_4, 0.05 M), and potassium chloride (KCl, 0.1 M). Sodium acetate was added to enhance buffering capacity to the pH 6.8. Throughout this manuscript, this formulation is denoted as PBS. PQ stock solution was prepared in 97% ethanol to obtain a final concentration of 4 mM. Glucose stock (1 M) was prepared in PBS using glucose (≥98%) and was left overnight to allow mutarotation before use. Potassium ferricyanide ($K_3[Fe(CN)_6]$) was prepared in distilled water at 0.5 M.

Gold nanoparticles (10 nm; OD 1) were purchased from Biotecha (Vilnius, Lithuania) as a citrate-stabilized suspension supplied by Sigma–Aldrich (Steinheim, Germany).

2.2. Yeast Preparation

Saccharomyces cerevisiae (commercial baker's yeast) was cultivated in YPD medium (50 g/L) prepared by dissolving 1 g of YPD powder in 20 mL of distilled water. Dried yeast (100 mg) was inoculated into the medium and incubated at 30 °C with shaking (200 rpm) until mid-log phase (20–24 h). Cells were harvested by centrifugation (3000× *g*,

5 min), washed three times with buffer (pH 6.8), and resuspended to 1.0 g/mL (wet mass) for electrode modification.

Polypyrrole-modified yeast (Sc:PPy) was prepared by in situ pyrrole polymerization on the cell surface following patent LT6239B [56] with minor adjustments. Yeast was incubated for 24 h at 30 °C (220 rpm) in buffer [56] containing 0.30 M pyrrole, 0.40 M potassium ferrocyanide, and 1.0 M glucose. After incubation, cells were harvested, washed, and resuspended as described above (1.0 g/mL).

Gold nanoparticle-decorated yeast (Sc:Au) was prepared by mixing the yeast suspension (1.0 g/mL) with the citrate-stabilized AuNP suspension (10 nm, OD 1) at a 1:1 (v/v) ratio and incubating for 10 min at room temperature with gentle mixing to promote AuNP adsorption. For the combined modification (Sc:PPy:Au), Sc:PPy cells were treated identically with AuNPs. Immediately after preparation, 4 µL aliquots of the corresponding yeast suspensions were drop-cast onto the working electrode as described in Section 2.3.

2.3. Graphite Electrode Preparation

Disposable graphite rod electrodes (25 mm length, 3 mm diameter; 99.995% trace metals basis) were cut, sequentially polished using abrasive papers up to P10000, rinsed with distilled water, and degreased with 97% ethanol. After drying in air, electrodes were used immediately for AuNP electrodeposition and/or biolayer immobilization.

Gold nanoparticles were deposited onto graphite rods (GR) by cyclic voltammetry in the commercial citrate-stabilized AuNP suspension (10 nm, OD 1) using a Metrohm µStat-i 400 potentiostat/galvanostat (Utrecht, The Netherlands) controlled by DropView 8400 M software in cyclic voltammetry (CV) mode. The potential was cycled between 0.0 and +1.0 V at 0.05 V s^{-1} for the desired number of cycles (10–70) to control AuNP loading. After deposition, electrodes were rinsed thoroughly with deionized water to remove weakly bound nanoparticles and used immediately. The chosen potential window was selected based on earlier reports on AuNP-modified graphite electrodes for glucose biosensing [57].

To facilitate electron mediation between the yeast layer and the electrode, 9,10-phenanthrenequinone (PQ) was used as a surface-confined redox mediator [44]. Unless stated otherwise, PQ (3 µL of 4 mM in ethanol) was drop-cast onto the polished (or AuNP-electrodeposited) graphite surface and allowed to dry before applying the yeast layer.

Yeast-based sensing layers were then formed by drop-casting 2 µL of the appropriate yeast suspension (Sc, Sc:PPy, 1.0 g/mL) or 4 µL of the appropriate yeast suspension (Sc:Au, Sc:PPy:Au; 1.0 g/mL) onto the PQ-modified electrode. The modification scheme is shown in Figure 1.

In the manuscript, electrodes are denoted as Sc (unmodified yeast), Sc:Au (AuNP-decorated yeast), Sc:PPy (PPy-modified yeast), and Sc:PPy:Au (PPy-modified yeast additionally decorated with AuNPs), with the prefix ecAu/GR used when the graphite substrate was additionally modified by electrochemical AuNP deposition.

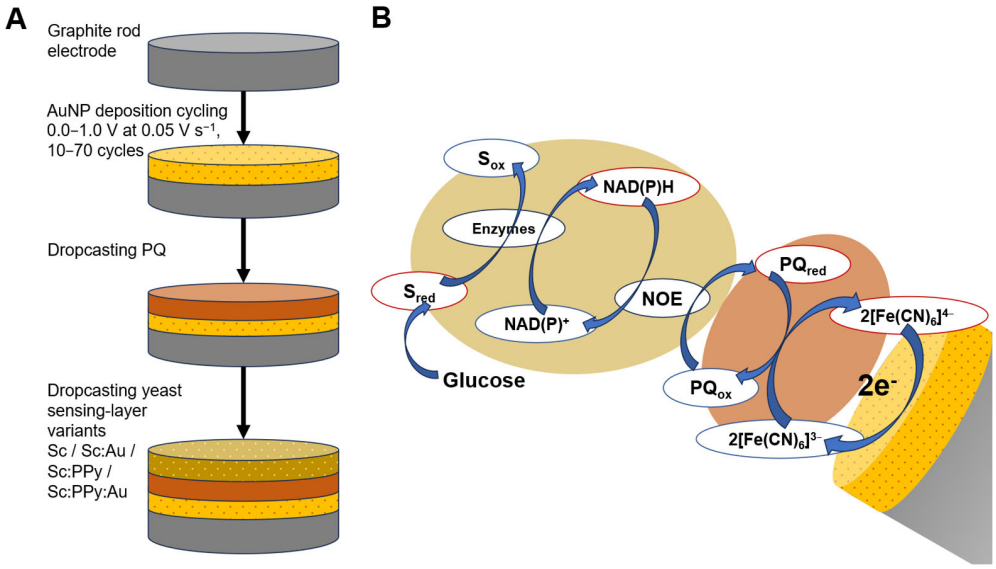


Figure 1. Electrode fabrication workflow and conceptual glucose-to-current transduction. (**A**) Preparation of AuNP-electrodeposited graphite electrodes followed by PQ immobilization and drop-casting of yeast sensing-layer variants (Sc, Sc:Au, Sc:PPy, Sc:PPy:Au). AuNP deposition was performed by CV (0.0–1.0 V, 0.05 V s^{-1}; 10–70 cycles). (**B**) Conceptual mediator-assisted mechanism: Glucose metabolism increases intracellular reducing power which is harvested via the immobilized quinone mediator (PQ) and the ferri-/ferrocyanide couple and collected as anodic current at the electrode.

2.4. Calculations

Electrochemical measurements were evaluated by using Hill's function:

$$J = \frac{V_{max} \times C^n}{k^n + C^n}, \quad (1)$$

where J is current density, C is the concentration of glucose, $Vmax$ is the maximal current density obtained at saturation, k is a constant, which is equal to substrate concentration at which half of maximal current is observed, and n is a Hill's coefficient. In this work, $Vmax$, k, and n are treated as apparent electroanalytical descriptors of glucose-to-signal transduction within the composite bioelectrode.

It is important to note that Equation (1) simplifies to the classical Michaelis–Menten expression when the Hill coefficient n is set to 1. Consequently, Hill fitting introduces an extra shape parameter (n), enabling the response curvature to differ from the rigid Michaelis-type assumption. In this study, n is considered an empirical descriptor of response nonlinearity (apparent cooperativity/heterogeneity) within the composite electrode–biolayer–mediator system, rather than serving as evidence of genuine biochemical binding cooperativity. In this parameterization, k denotes the apparent half-saturation concentration, indicating the glucose level at which approximately 50% of the fitted maximum signal is attained. This serves as a practical descriptor of the response affinity and dynamic range of the electrode configuration under the specified measurement conditions. The parameter $Vmax$ represents the fitted upper-limit signal at elevated glucose levels (signal capacity), facilitating the comparison of the maximum achievable current density across different modification states. When considered collectively, the reporting of ($Vmax$, k, n) facilitates comparisons between electrodes regarding both saturation levels and response curvature through a unified, internally consistent model, without suggesting a particular molecular binding mechanism.

Surface roughness was evaluated using *Ra* and *Rq* parameters derived from AFM data. The arithmetic average *Ra*:

$$R_a = \frac{1}{L}\int_0^L |Z(x)|dx, \quad (2)$$

The root-mean-square (RMS) roughness *Rq*:

$$R_q = \sqrt{\frac{1}{L}\int_0^L |Z^2(x)|dx}, \quad (3)$$

where $Z(x)$ represents the function that characterizes the surface profile in relation to height (Z) and position (x) across the assessed length (L).

The limit of detection (LOD) was calculated using the 3σ criterion [58],

$$LOD = \frac{3\sigma}{\text{slope}}, \quad (4)$$

where σ is the standard deviation of the blank (baseline) response and the slope was taken from the low-concentration calibration fit.

2.5. Atomic-Force-Microscopy-Based Measurements

The BioScope II AFM, combined with an inverted optical microscope developed by Veeco Instruments Ltd. (Santa Barbara, CA, USA) and an NP-D cantilever (Bruker, Camarillo, CA, USA) was used for the measurements. AFM contact mode was applied at 0.15 Hz. Raw data were analysed using NanoScope Analysis 1.5 software.

2.6. Electrochemical Measurements

Electrochemical measurements were conducted with a Metrohm μStat-i 400 potentiostat/galvanostat (Utrecht, The Netherlands) controlled by DropView 8400 M software at ambient temperature (20 °C). A conventional three-electrode configuration was used, comprising a graphite working electrode, a platinum counter electrode, and an Ag/AgCl reference electrode (3 M KCl). The borosilicate glass titration vessel (with plastic mounting ring and lid), as well as the platinum and 12.5 cm Ag/AgCl (3 M KCl) electrodes, were purchased from Metrohm AG (Herisau, Switzerland). When changes in glucose or other reagent concentrations were required, they were introduced stepwise by sequential addition to the same electrochemical cell.

For each experiment, cyclic voltammetry was recorded over ten consecutive cycles between −0.35 V and +0.70 V at a scan rate of 0.1 V s^{-1} with a 2 mV potential step. Only the final cycle is shown in the figures.

EIS measurements of the graphite electrodes was performed using Metrohm Autolab PGSTAT302N (Utrecht, The Netherlands), employing a 3 electrode cell filled with 2.5 mM $K_3[Fe(CN)_6]/K_4[Fe(CN)_6]$ solution in PBS and 0.1 M KCl supporting electrolyte, where the graphite electrode was used as a working electrode, a Ag/AgCl (3 M KCl) was used as a reference electrode, and a Pt rod counter electrode. The potentiostatic EIS measurement was performed at OCP (0.25 V), applying 10 mV perturbation sine signals at frequencies ranging from 100 kHz to 20 mHz, distributed logarithmically, 10 points per decade (68 points). EIS data were fitted using Zview 2 software. EIS characterization was performed only for abiotic electrodes to enable a direct comparison of the AuNP modification effect. Yeast immobilization introduces additional heterogeneous and time-dependent interfacial contributions that complicate cross-condition interpretation.

3. Results

3.1. Evaluation of AuNP Deposition Method

3.1.1. Evaluation of Electrode Morphological Properties and Surface

Bare graphite and electrochemically deposited AuNP on graphite electrodes were examined using AFM to measure the changes in surface topography caused by the deposition process (Figure 2). The process of electrodeposition resulted in an increase in RMS roughness (*Rq*) from 66.6 to 96.7 nm, reflecting a 1.45-fold increase (+45.2%) (Table 1). Similarly, the average roughness (*Ra*) elevated from 56.6 to 79.6 nm, indicating a 1.41-fold increase (+40.6%). The height range increased from 326 to 598 nm (1.83-fold; +83.4%), demonstrating a significant enhancement in topographic amplitude following deposition. Simultaneously, the difference in surface area rose from 0.00594% for bare graphite to 1.14% after the deposition of AuNP, indicating an approximate 192-fold increase (≈+19,100%), which aligns with a significantly more textured surface. This increase signifies geometric surface roughening. However, it does not automatically imply a greater electrochemically active area for faradaic mediator exchange. Dense coverage may still obscure micropores and edge sites, thereby limiting local transport.

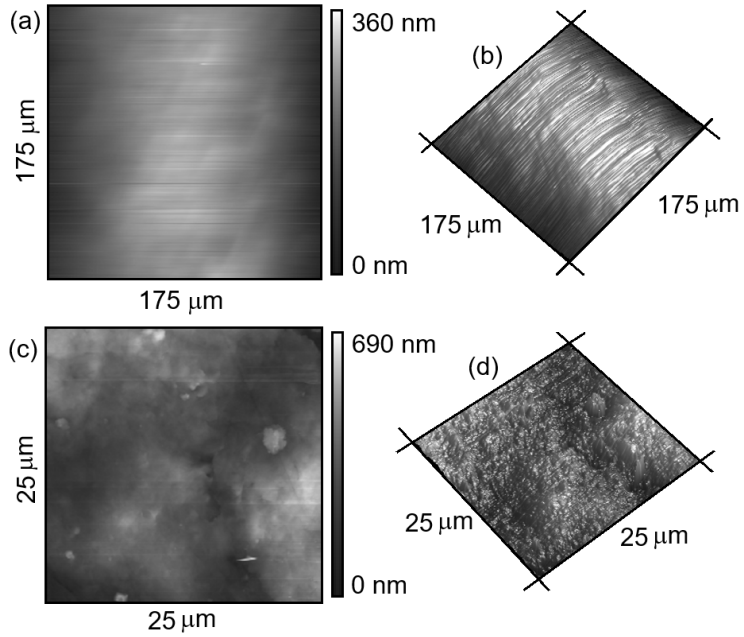


Figure 2. AFM topography of graphite electrodes before and after AuNP electrodeposition. (**a**) Unmodified graphite 2D view; (**b**) unmodified graphite 3D view; (**c**) graphite modified by AuNP 2D view; (**d**) graphite modified by AuNP 3D view.

Table 1. Parameters of surface topography of unmodified and AuNP modified graphite.

Parameter	Graphite	Graphite Modified by AuNP	Difference
Rq	66.6	96.7	+45.2%
Ra	56.6	79.6	+40.6%
Height range	326	598 nm	+83.4%
Surface area difference	0.00594%	1.14%	+19,100%

AFM imaging was used to examine the surface morphology of Saccharomyces cerevisiae cells before and after AuNP modification (Figure 3). The unmodified yeast cells exhibited a relatively smooth and continuous surface in the 3D view (Figure 3a). After

AuNP treatment, the yeast surface showed increased topographical heterogeneity and the appearance of nanoscale features consistent with nanoparticle adsorption, visible in both the 8 µm × 8 µm scan (Figure 3b) and the higher-resolution 2 µm × 2 µm scan (Figure 3c). The corresponding 2D height map (Figure 3d) further confirms the presence of localized height variations associated with the modified surface. These observations verify that AuNPs were successfully introduced onto the yeast surface prior to electrochemical measurements.

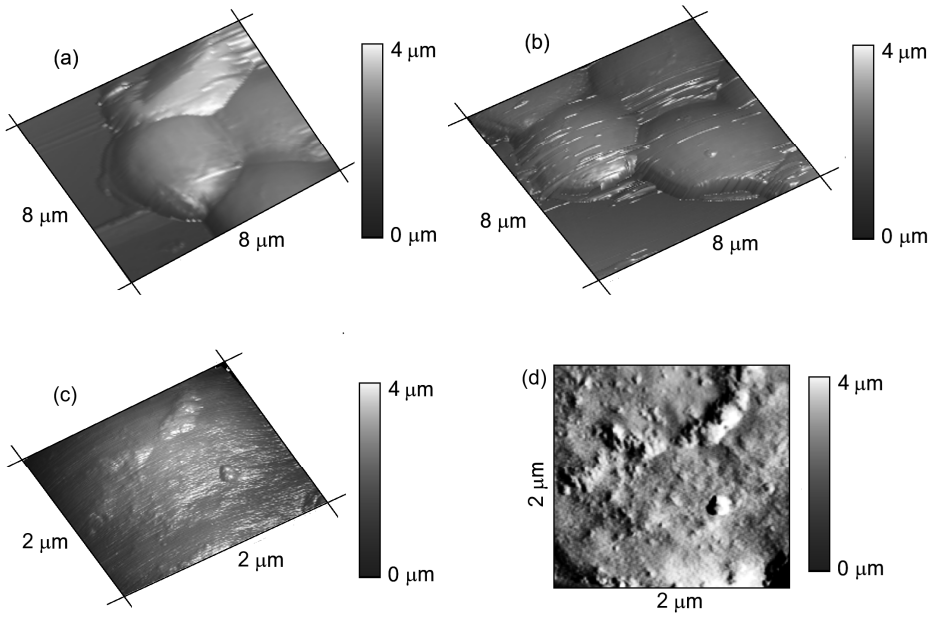


Figure 3. AFM topography of yeast cells before and after AuNP modification. (**a**) Unmodified yeast cells 3D view; (**b**) AuNP-modified yeast 3D view; (**c**) corresponding 2D height map (**d**). Scale bars and height (z) scales are indicated in each panel.

3.1.2. Deposition Cycle Numbers' Impact on the Electrode Electrochemical Properties

The impact of the number of cycles in the electrochemical deposition method on the electrochemical behavior of the electrode was assessed through cyclic voltammetry (Figure 4). This was carried out using electrochemically deposited yeast-based electrodes in buffer with glucose concentrations varying from 0 to 60 mM, alongside 30 mM potassium ferricyanide ($K_3[Fe(CN)_6]$). The choice of 30 mM potassium ferricyanide was informed by prior experimental findings, which indicated a distinct linear relationship between mediator concentration and current density within the 10–50 mM range for unmodified electrodes [13]. The concentration of the mediator set at 30 mM was thus chosen to facilitate a stable, glucose-dependent faradaic response within the linear mediator-response region, allowing for reliable comparison of analytical signal variations across different glucose levels while circumventing mediator-limited or saturated conditions.

Across all cycle numbers, the glucose-response curves showed a saturating, non-linear dependence over the examined concentration range. The glucose-response curves were fitted using the Hill function (Equation (1)) to allow consistent comparison of saturation behavior across electrode variants.

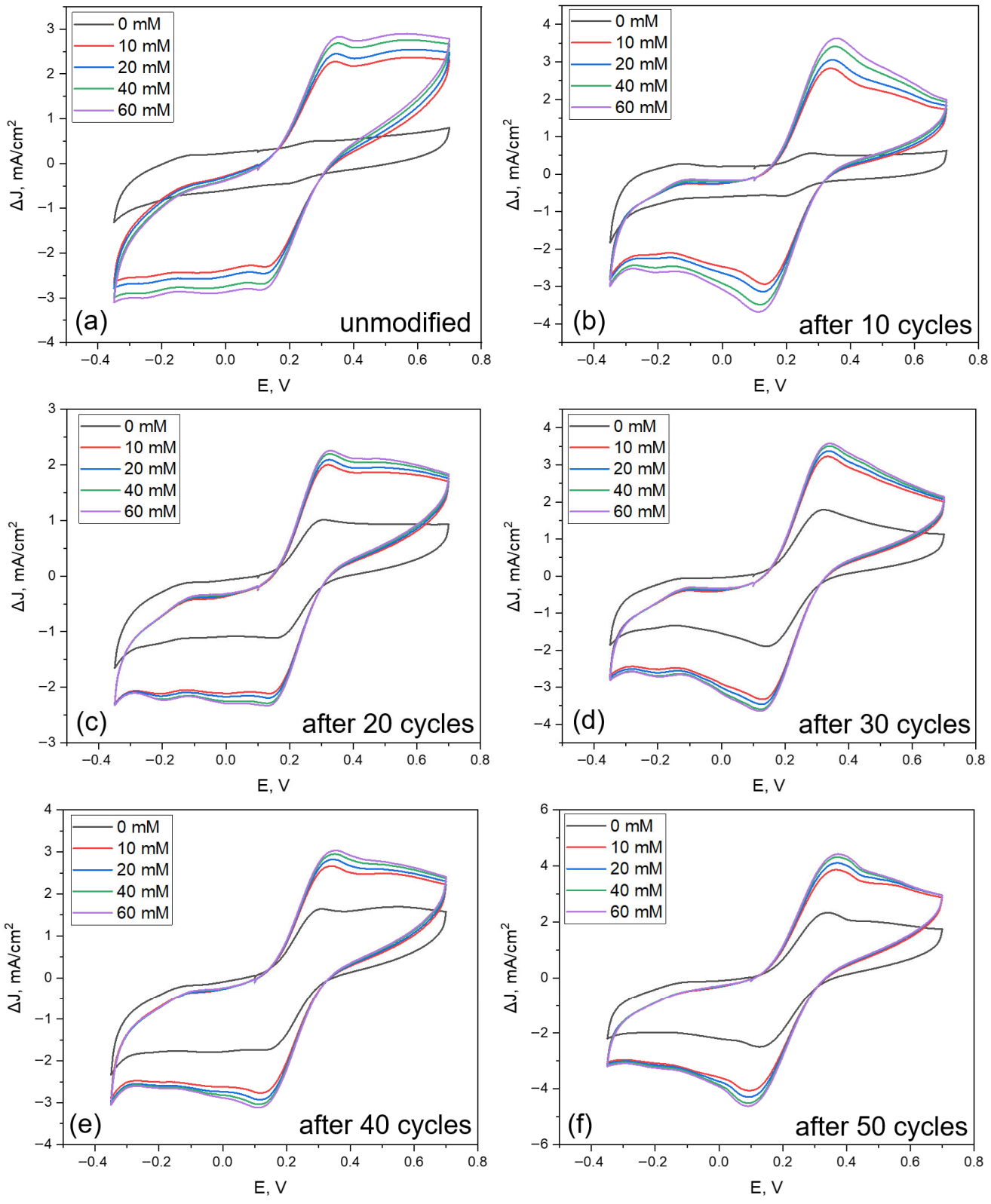


Figure 4. *Cont.*

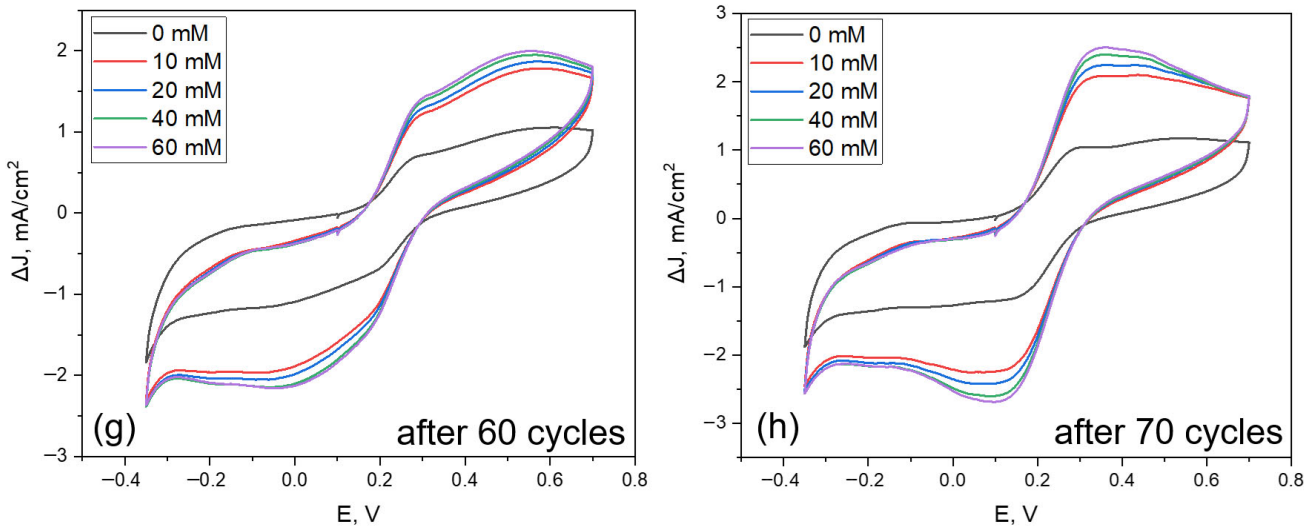


Figure 4. Cyclic voltammograms registered using unmodified (**a**), 10 (**b**), 20 (**c**), 30 (**d**), 40 (**e**), 50 (**f**), 60 (**g**), and 70 (**h**) cycles electrodeposited AuNP graphite electrode at different glucose concentrations in 30 mM potassium ferricyanide ($K_3[Fe(CN)_6]$). Scan rate of 0.1 V/s, and a step size of 2 mV was applied.

The electrodes modified with electrochemically deposited AuNP showed a significant dependence of kinetic parameters on the number of deposition cycles (Table 2, Figure 5). During the initial cycles (10–30 cycles), remarkably high k values (3454.75, 377.67, and 47.45 mM, respectively) were recorded, suggesting slow apparent kinetics and restricted accessibility of electroactive sites. The electrodes exhibited notably low Hill coefficients ($n \approx 0.20$–0.24), indicative of negative cooperativity, suggesting that an increase in glucose concentration does not lead to a proportional enhancement in electrochemical signal (Table 2).

Table 2. The determined half-saturation constant (k) and Hill coefficient (n) on electrodes modified with electrochemically deposited AuNP.

Cycles	V_{max}, mA/cm^2	k, mM	n
10	11.01	3454.75	0.24
20	3.43	377.67	0.20
30	3.5	47.45	0.22
40	1.67	5.08	0.63
50	4.84	162.84	0.27
60	2.0	493.97	0.29
70	4.47	1660.01	0.23
Control	3.39	8.80	0.40

A notable shift was observed at 40 deposition cycles, with the k value dropping significantly to 5.08 mM, exceeding the kinetic performance of the unmodified control electrode (k = 8.80 mM). At the same time, the Hill coefficient rose to 0.63, suggesting a partial reduction in negative cooperativity and enhanced functional coupling among electroactive sites. Although the absolute peak currents at high glucose can appear similar to the control in Figure 5, the fitted response curvature and half-saturation behavior differ, particularly at low-to-intermediate glucose concentrations.

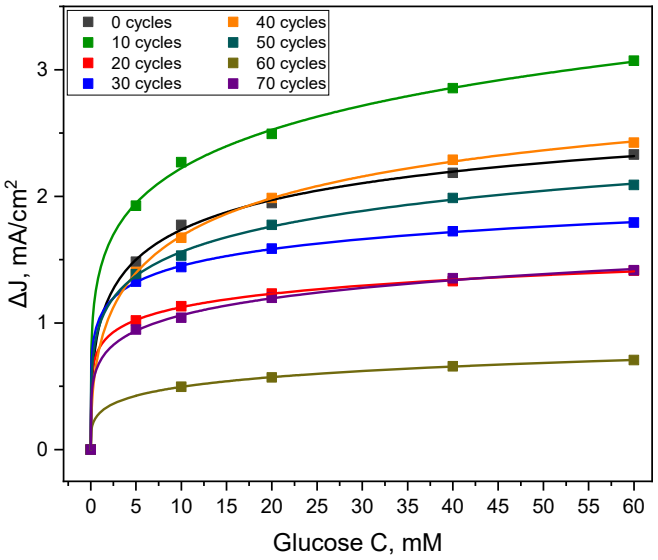


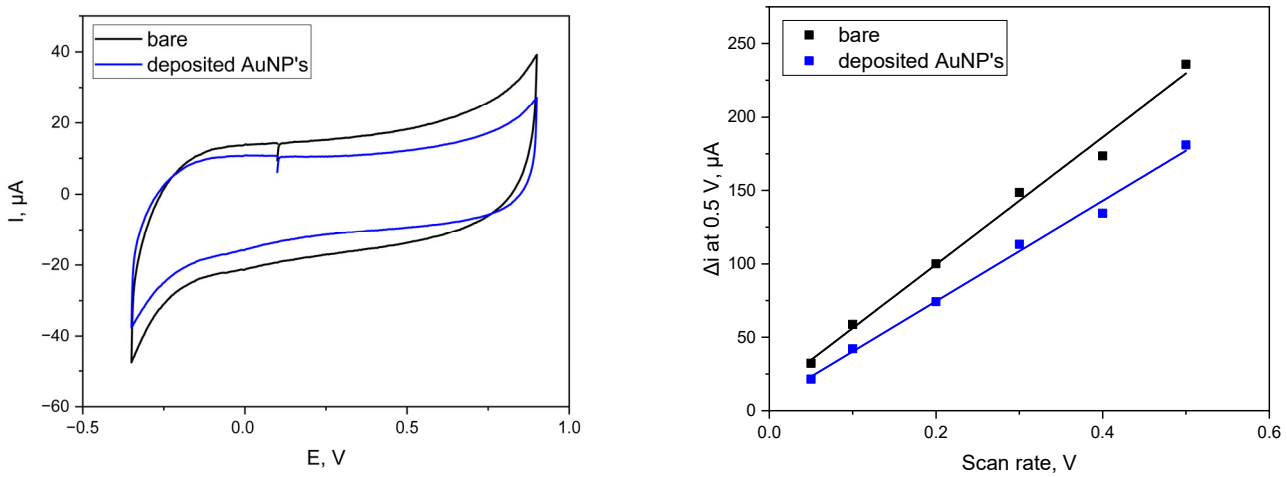
Figure 5. An amount of 30 mM potassium ferricyanide ($K_3[Fe(CN)_6]$) oxidation peaks from voltammograms in Figure 4 as a dependency of glucose concentration on electrodes modified with a different number of AuNP electrodeposition cycles.

Nonetheless, additional increments in deposition cycles (50–70 cycles) led to a reversal of this pattern. The *k* values exhibited a significant increase to 162.84, 493.97, and 1660.01 mM, respectively, while the Hill coefficients reverted to lower values ($n \approx 0.23$–0.29).

The fitted *Vmax* values demonstrate a significant, non-linear relationship with the number of AuNP electrodeposition cycles: the electrode with 10 cycles shows the highest *Vmax* (11.01), which is succeeded by a notable decline at 20–40 cycles (*Vmax* = 3.43–1.67), and a partial recovery at 50–70 cycles (*Vmax* = 2.00–4.84), in contrast to the control (Vmax = 3.39). This behavior indicates that the deposition of AuNP affects not only the observed half-saturation behavior (*k*) but also the maximum achievable current, which may be constrained by alterations in the effective electroactive surface area, interfacial electron-transfer pathways, and/or mass transport within the modified layer. 40 cycle electrodeposition variants seem to indicate an ideal equilibrium between nanoparticle coverage and surface accessibility, promoting more effective electron transfer, and producing the most favorable glucose responsiveness across the evaluated electrodeposition conditions. Accordingly, all subsequent measurements were performed using this modification.

3.1.3. Cyclic Voltammetry of Bare and AuNP-Modified Graphite Electrodes in PBS

Cyclic voltammetry was performed on bare graphite electrodes and AuNP-modified graphite electrodes through electrochemical deposition in phosphate-buffered saline at scan rates ranging from 0.05 to 0.5 V s^{-1} (Figure 6a). Due to the absence of any redox-active species or mediators in the electrolyte, there were no observable faradaic oxidation or reduction peaks for any of the electrode configurations. In these circumstances, the observed current response is primarily influenced by non-faradaic processes, notably electric double-layer charging and interfacial capacitive effects [59,60]. The characterization of capacitive response is crucial for understanding how background currents influence baseline and noise in electrochemical sensing, particularly when interpreting signal-to-background behavior in mediator-assisted glucose measurements.



(**a**) (**b**)

Figure 6. (**a**) Cyclic voltammograms in PBS of unmodified and AuNPS-modified graphite electrode at 0.05 V scan rate. (**b**) Δi at different scan rates.

To facilitate quantitative comparison under these conditions, the current recorded at 0.5 V was extracted from both the forward and reverse scans. The difference between these values (Δi) served as a metric to assess capacitive behavior and interfacial charge-relaxation dynamics. The dependence of Δi on scan rate offers valuable insights into surface uniformity, electronic connectivity, and interfacial resistance [61–63], that pertain to background stability and baseline drift in biosensing-type readouts.

The current magnitude exhibited a linear increase with the scan rate across both electrode configurations, aligning with capacitive behavior (Figure 6b). As a result, Δi exhibited an increase with the rising scan rate across both electrodes. The bare graphite electrode showed the most significant widths throughout the entire scan-rate range, rising from 32.27 µA at 0.05 V s^{-1} to 235.96 µA at 0.5 V s^{-1}, indicating marked charging–discharging asymmetry and a slower interfacial charge equilibration process. The modification of AuNP led to a decrease in Δi across all scan rates. Electrochemically deposited AuNP electrodes demonstrated the smallest Δi, which increased from 21.58 µA to 180.98 µA across the same scan-rate range.

3.1.4. EIS Study of AuNP Modified Electrodes

The EIS measurement result of the bare and AuNP-modified graphite electrode is presented in Figure 7. The resulting data was fitted using a modified Randles equivalent circuit model, which consists of solution resistance Rs, charge transfer resistance Rct, constant phase element of the double electric layer at the graphite-electrolyte interphase CPE, and Warburg semi-infinite diffusion element W (Table 3). In the classical Randles model, an ideal capacitor is used to model double electric layer capacitance at the electrode-solution interface, but herein we instead use CPE to account for surface inhomogeneity [64]. Only the semi-circular part with a diffusion "tail" was interpreted using the circuit model to observe the changes in the interfacial region of the electrode. From a biosensing perspective, these parameters are crucial as they influence background charging behavior, interfacial transport, and the efficiency and reproducibility of mediator-driven signal transduction [65].

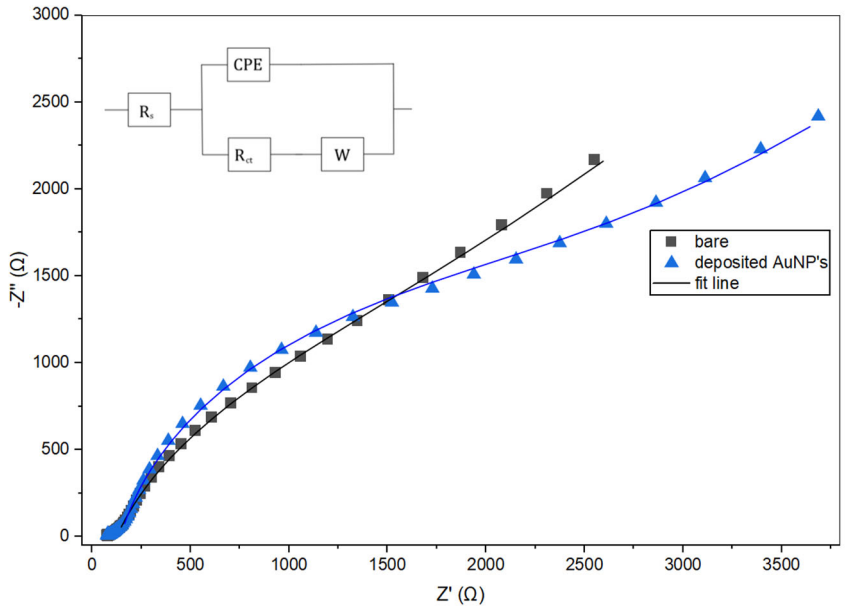


Figure 7. Nyquist graph of unmodified graphite (black squares), graphite electrode modification via electrochemical deposition (blue triangles); line—fit line of the modified-Randles equivalent circuit model (inset).

Table 3. Modified-Randles equivalent circuit model fit results for the used elements; σ denotes standard deviation for triplicate experiments.

Electrode	R_{ct}, Ω	σ (R_{ct})	CPE, mS × s^n	σ (CPE)	*n*	σ (*n*)	W, mS × $s^{1/2}$	σ (W)
Bare graphite	1592	252.5	0.536	0.0246	0.785	0.00511	0.871	0.0565
Deposed AuNP's on GR	2617	145.2	0.319	0.0177	0.863	0.0240	0.925	0.0373

After the AuNP modification, an increase in charge transfer resistance was observed (Table 2, AuNP-modified electrode exhibited *R*ct = 2617 Ω compared to 1592 Ω for bare graphite). This could be attributed to partial graphite micropore blocking by AuNPs [66], which can reduce the fraction of highly active graphite sites accessible for mediator-driven charge transfer, thereby increasing the apparent interfacial resistance.

Concurrently, the CPE exponent *n* rose from 0.785 to 0.863 following the deposition of AuNP, indicating an enhancement in surface homogeneity and a more confined distribution of relaxation times. In this context, a higher *n* value indicates that the electrode response exhibits reduced structural dispersion, aligning more closely with an ideal capacitive element. This change aligns with a more consistent interfacial electrical response, which is beneficial for biosensor functionality, particularly where signal reliability and drift management are essential. These trends suggest that the deposition of electrochemical AuNP could enhance the uniformity of the electrode–electrolyte interface.

3.2. Electroanalytical Assessment of Yeast-Based Sensing Layers on Gold Nanoparticle-Electrodeposited Graphite Electrodes

Four yeast configurations were analyzed alongside AuNP-modified graphite electrodes: unmodified yeast (Sc), yeast modified with gold nanoparticles (Sc:Au), yeast modified with polypyrrole (Sc:PPy), and yeast modified with both polypyrrole and gold nanoparticles (Sc:PPy:Au). When these yeast layers are immobilized on AuNP-electrodeposited graphite, the notation becomes Sc/ecAu/GR, Sc:Au/ecAu/GR, Sc:PPy/ecAu/GR, and Sc:PPy:Au/ecAu/GR.

To examine the glucose-dependent electroanalytical response, cyclic voltammetry was carried out using glucose concentrations from 0 to 60 mM in the presence of 30 mM potassium ferricyanide. Cyclic voltammetry demonstrated that electrochemical deposition (ecAu) modified electrodes displayed distinct mediator redox responses influenced by the yeast modification strategy and the availability of glucose. The anodic peak current densities for ecAu-based electrodes in glucose-free electrolyte varied from 1.12 to 2.68 mA·cm^{-2}, with oxidation peak potentials observed between 0.29 and 0.37 V (Figure 8). The Sc/ecAu/GR electrode exhibited the highest baseline anodic current density (2.50 mA·cm^{-2} at 0.37 V) (Figure 8a).

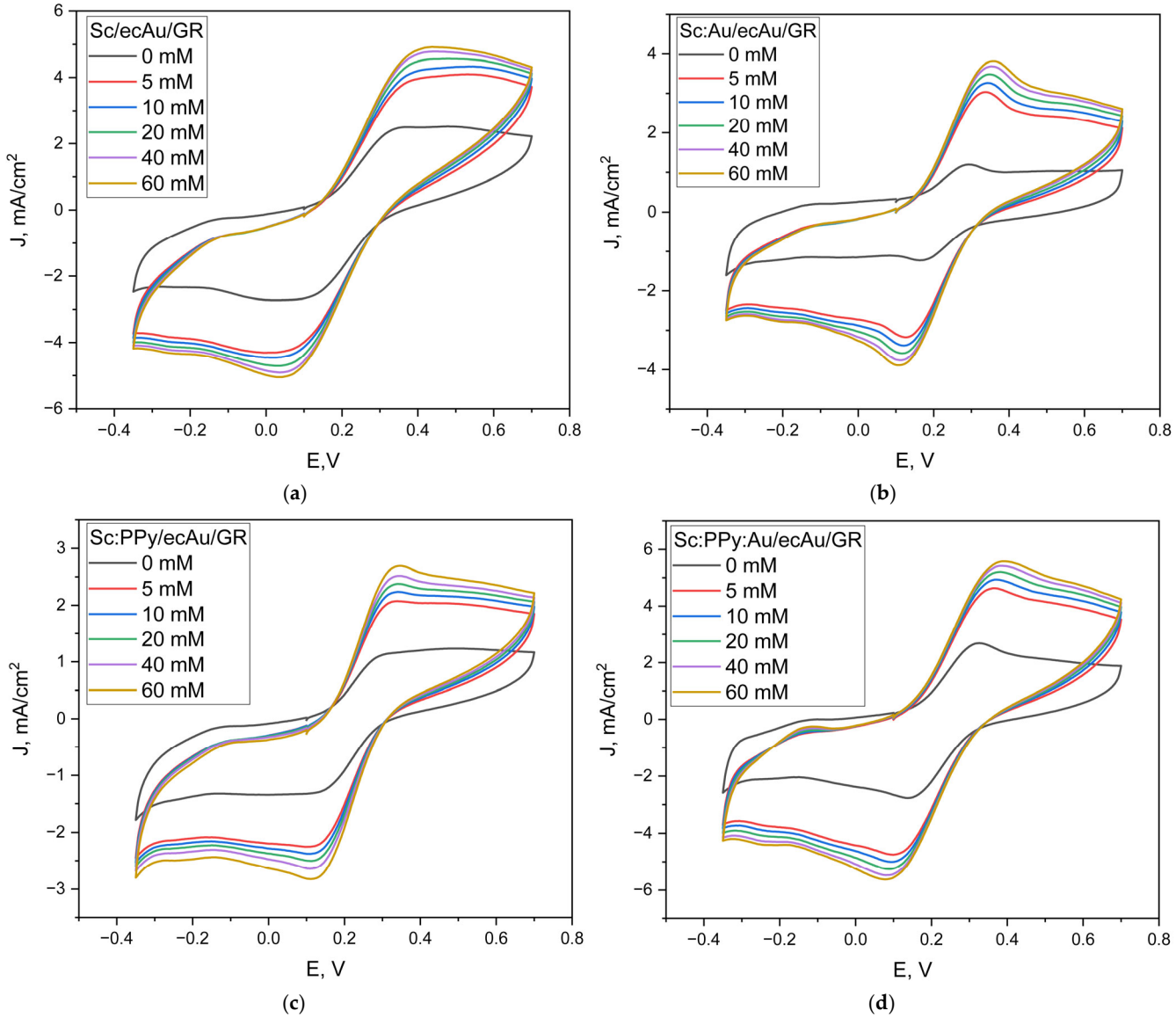


Figure 8. Cyclic voltammograms registered using different AuNP-modified electrodes by electrochemical deposition configurations: (**a**) a graphite electrode modified only with yeast (Sc/ecAu/GR), (**b**) Sc:Au-modified graphite electrode (Sc:Au/ecAu/GR), (**c**) graphite electrode modified only with PPy modified yeasts (Sc:PPy/ecAu/GR) and (**d**) Sc:PPy:Au-mixture-modified graphite electrode (Sc:PPy:Au/ecAu/GR) at different glucose concentrations in the buffer solution. A scan rate of 0.1 V/s and a step size of 2 mV were applied.

In contrast, the Sc:Au/ecAu/GR (Figure 8b) and Sc:PPy/ecAu/GR (Figure 8c) electrodes demonstrated lower baseline anodic currents (1.19 and 1.12 mA·cm^{-2}, respectively), indicating that the modification of yeast surfaces, especially with polypyrrole, introduces

additional film resistance and/or diffusion limitations that inhibit background mediator currents in the absence of glucose. Significantly, the Sc:PPy:Au/ecAu/GR (Figure 8d) electrode not only restored but also slightly surpassed the baseline performance of the unmodified yeast system, achieving 2.68 mA·cm^{-2} at 0.33 V.

With the introduction of 60 mM glucose, all ecAu-based electrodes exhibited a distinct increase in anodic current density consistent with glucose-driven enhancement of mediator turnover, along with positive shifts in the oxidation peak potential. The Sc/ecAu/GR electrode showed an increase from 2.50 to 4.92 mA·cm^{-2}, while the oxidation peak shifted from 0.37 to 0.44 V. A comparable trend was noted for Sc:Au/ecAu/GR, which rose from 1.19 to 3.81 mA·cm^{-2} and shifted from 0.29 to 0.36 V.

The Sc:PPy/ecAu/GR electrode exhibited the least pronounced anodic response when glucose was introduced, rising merely to 2.69 mA·cm^{-2} at 0.35 V, which aligns with restricted charge transport and/or restricted mediator/analyte availability due to the polymer-dense biolayer. The Sc:PPy:Au/ecAu/GR electrode demonstrated the most significant glucose-induced enhancement among ecAu systems, achieving a current density of 5.58 mA·cm^{-2} at 0.39 V.

The analysis of the cathodic peak provided additional support for these findings. Without glucose, cathodic current densities varied between −1.23 and −2.77 mA·cm^{-2}, transitioning to −2.83 to −5.63 mA·cm^{-2} when 60 mM glucose was present. The most significant cathodic response was once more noted for the Sc:PPy:Au/ecAu/GR electrode (−5.63 mA·cm^{-2} at 0.078 V), showing improved mediator regeneration and better redox reversibility, which benefits consistent amperometric/voltammetric sensing results.

3.3. Kinetic Evaluation of Yeast-Based Biosensing Layers

To analyze the glucose response within an electroanalytical (biosensing) framework, the anodic peak current density associated with the ferricyanide-mediated oxidation process was utilized as the analytical signal and assessed in relation to glucose concentration (0–60 mM) under consistent electrolyte and scan conditions (Table 4, Figure 9). In all yeast configurations immobilized on electrochemically deposited AuNP on graphite, an increase was observed with rising glucose concentration. However, it gradually diverged from a linear relationship and neared saturation at elevated substrate concentrations. This behavior aligns with mediator-assisted bioelectrocatalysis at immobilized biolayers, where the measurable signal is ultimately constrained by a limited number of accessible electroactive sites and by transport/permeability limitations within the interfacial layer [67].

Table 4. The determined half-saturation constant (*k*) and Hill coefficient (*n*) on differently modified electrodes.

Configuration	*Vmax*	*k*	*n*
Sc/ecAu/GR	3.62	5.08 mM	0.63
Sc:Au/ecAu/GR	3.87	6.28 mM	0.34
Sc:PPy/ecAu/GR	14.12	1.39 mM	0.21
Sc:PPy:Au/ecAu/GR	3.75	4.14 mM	0.45

Considering the inherently non-linear response throughout the entire 0–60 mM range, the concentration dependence was evaluated using Hill's equation (Equation (1)), serving as a concise empirical model. Within this framework, *Vmax* reflects the maximal current density at saturation (signal capacity), *k* denotes the concentration at which approximately 50% of the maximal response is achieved, whereas *n* reflects whether the incremental signal gain is enhanced ($n > 1$) or gradually attenuated ($n < 1$) as glucose levels rise. In the series of electrochemically deposited samples, all yeast variants demonstrated $n < 1$ (0.21–0.63),

suggesting a sub-linear response regime where the incremental increase in current density diminishes as glucose concentration increases (Figure 9). The Sc/ecAu/GR configuration exhibited a relatively balanced performance ($Vmax$ = 3.62, k = 5.08 mM, n = 0.63). The direct introduction of AuNPs to yeast resulted in a shift in the response, indicating a weaker concentration dependence (Sc:Au/ecAu/GR, $Vmax$ = 3.87, k = 6.28 mM, n = 0.34). The Sc:PPy/ecAu/GR electrode exhibited the most significant deviation from proportionality, with $Vmax$ = 14.12, k = 1.39 mM, n = 0.21, indicating a substantial maximal fitted signal accompanied by notable curvature that aligns with transport and permeability limitations within the polymer-containing layer. The integration of AuNPs into the PPy-modified yeast partially mitigated this limitation (Sc:PPy:Au/ecAu/GR, $Vmax$ = 3.75, k = 4.14 mM, n = 0.45), indicating enhanced electronic and transport connectivity within the composite sensing layer, while preserving a non-linear calibration profile overall.

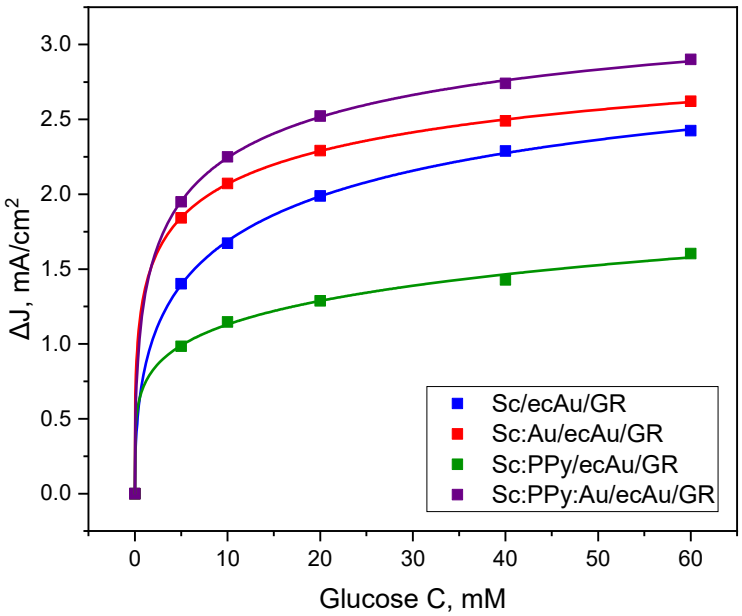


Figure 9. Oxidation peaks of current from voltammogram as a dependency on glucose concentration on electrodes modified with electrochemically deposited AuNP.

3.4. Calibration Characteristics

The glucose-dependent responses are non-linear over the full investigated range (0–60 mM). For practical readout in the low-glucose region, an empirical working calibration was additionally evaluated between 1 and 10 mM by plotting ΔJ as a function of ln(C) (Figure 10). In this range, the response could be approximated by $\Delta J = a \cdot \ln(C) + b$, yielding: Sc:Au/ecAu/GR, $\Delta J = 0.943 \cdot \ln(C) + 0.075$ (R^2 = 0.962); Sc:PPy/ecAu/GR, $\Delta J = 0.5181 \cdot \ln(C) + 0.0349$ (R^2 = 0.9725); Sc:PPy:Au/ecAu/GR, $\Delta J = 1.0182 \cdot \ln(C) + 0.0718$ (R^2 = 0.9699); and Sc/ecAu/GR, $\Delta J = 0.7522 \cdot \ln(C) + 0.0444$ (R^2 = 0.9787) (Table 5). The limits of detection (LOD) were calculated using Equation (4), giving 1.016 mM (Sc:Au/ecAu/GR), 1.330 mM (Sc:PPy/ecAu/GR), 0.540 mM (Sc:PPy:Au/ecAu/GR), and 3.360 mM (Sc/ecAu/GR), indicating that the combined PPy–AuNP yeast modification provides the most favorable low-range detectability within this dataset. Because the low-range calibration is based on three concentration levels (1, 5, and 10 mM), these ln(C) fits are presented as an empirical working calibration for the low-glucose regime, while the Hill fit remains the primary descriptor across the full 0–60 mM range.

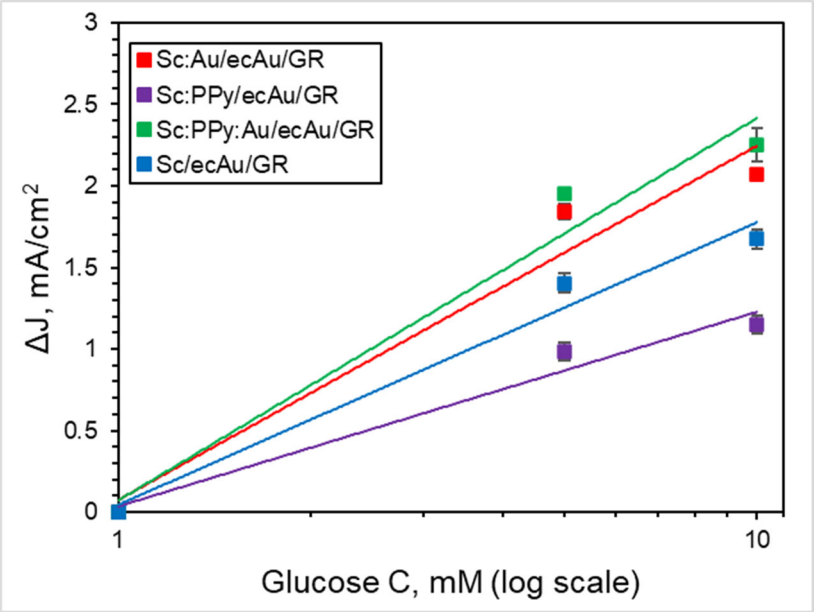


Figure 10. Low-range glucose calibration (1–10 mM). Anodic peak current density change (ΔJ) for yeast-modified ecAu/GR electrodes as a function of glucose concentration in the low-concentration regime. Lines show empirical logarithmic fits (ΔJ = a·ln(C) + b) used for comparative calibration and LOD estimation.

Table 5. Calibration parameters for the equation ΔJ = a·ln(C) + b.

Configuration	a	b	R^2	LOD
Sc:Au/ecAu/GR	0.943	0.075	0.962	1.016 mM
Sc:PPy/ecAu/GR	0.5181	0.0349	0.9725	1.330 mM
Sc:PPy:Au/ecAu/GR	1.0182	0.0718	0.9699	0.540 mM
Sc/ecAu/GR	0.7522	0.0444	0.9787	3.360 mM

4. Discussion

The electrochemical behaviour of the modified electrodes is interpreted by combining AFM-derived structural information with complementary electrochemical characterization. The structural foundation for these electrochemical changes is provided by AFM. The observed increases in *Ra*/*Rq*, height range, and surface development indicate that electrodeposition generates a more textured graphite surface through the formation of additional asperities and increased height variability. It is crucial to note, however, that greater geometric roughness does not automatically ensure enhanced electroactive accessibility: a surface that is rough yet densely covered may still exhibit elevated *Rct* if deposition obstructs edge-plane activity, fills microfeatures, or creates a denser interphase that restricts local mediator penetration. At the same time, the enhanced nanoscale texture can increase the density of interfacial features and improve wetting, which may reinforce mediator/electrolyte access and stabilize analyte-dependent faradaic responses. Such topographical restructuring is also expected to modify the local electric-field distribution, thereby influencing charge accumulation and relaxation behavior and, consequently, baseline currents, interfacial impedance, and the consistency of electrochemical readouts. Therefore, AuNP deposition may increase geometric texture/roughness while still increasing *Rct* if the deposition screens fast electron-transfer sites or restricts local mediator transport. These structural changes are consistent with the electrochemical behavior observed in cyclic voltammetry and impedance measurements.

Electrochemical AuNP deposition modified the graphite interphase in a cycle number-dependent manner, producing large shifts in the fitted glucose-response parameters (*k*, *n*, *Vmax*). Sparse or uneven AuNP coverage at low cycle numbers does not effectively create efficient electron-transfer pathways between the redox mediator, glucose, and the electrode surface, thereby limiting glucose-dependent signal amplification. A moderate loading of AuNP enhances electronic coupling and stabilizes the interfacial response, while excessive electrochemical deposition results in nanoparticle aggregation, surface passivation, or mass-transport limitations, all of which collectively diminish effective electron exchange. This level of over-modification probably hinders mediator diffusion and obstructs active sites, underscoring the limited operational range linked to electrochemical AuNP deposition, and narrowing the useful analytical response window for glucose sensing. This pattern aligns with nanostructured bioelectrodes, where the incorporation of conductive nanofeatures can improve wiring and connectivity. However, an overabundance of coverage may hinder pore and edge domains, creating diffusion barriers in mediator-assisted systems [66–72].

The lack of faradaic peaks in mediator-free PBS indicates that the response is primarily governed by double-layer charging [58,59]. The reduced hysteresis width (Δi) following AuNP deposition indicates a quicker and more uniform charge accumulation and relaxation, aligning with enhanced electronic continuity at the interface and diminished charging lag [61–63]. The EIS results indicate that the deposition of AuNP leads to an increase in Rct, which can adversely affect sensitivity by restricting mediator exchange kinetics, especially at low analyte concentrations where minor signal variations need to be distinguished from background currents. The change in CPE values for the electrodes modified through electrochemical AuNP deposition reveals a distinct modification of the electrode–electrolyte interfacial structure. The CPE showed a significant decrease compared to bare graphite, indicating a reduction in the apparent double-layer (pseudo)capacitance at the interface. Decreased interfacial (pseudo)capacitance could be advantageous by diminishing non-faradaic background contributions and enhancing baseline stability, although the observed decrease could be linked to the partial coverage of graphite microfeatures that play a significant role in capacitive charging, or it may result from the development of a denser interfacial layer that restricts charge accumulation during small-signal perturbations. This suggests a tighter distribution of relaxation times and a more uniform interphase, despite the presence of some electroactive microdomains that may be screened or partially blocked [64–67]. The observed trends suggest that electrodeposition has the potential to diminish heterogeneity in the electrical response, all the while effectively narrowing the proportion of graphite sites that remain ideally accessible for mediator exchange.

The yeast-layer data suggest that the formation of signals is influenced by the interaction between the electrodeposited AuNP interphase and the permeability and conductivity of the immobilized yeast film. Unmodified *Saccharomyces cerevisiae* was initially utilized as a standardized biological sensing layer to evaluate the AuNP deposition method on a graphite electrode, and to establish a reproducible mediator-based electrochemical baseline. This approach offered valuable insights into the effects of electrochemical deposition integration of AuNPs on electrode conductivity and redox behavior. However, it fails to completely encompass the mechanisms involved in the formation of the analytical signal at a yeast–electrode sensing interface. The current recorded in mediator-assisted electrochemical biosensing is influenced by the properties of the electrode as well as the physicochemical structure of the immobilized biolayer. Additionally, factors such as the biolayer's permeability to the mediator/analyte and the efficiency of interfacial charge transfer within the film play significant roles.

To overcome this limitation and improve electroanalytical performance, further experiments implemented specific modifications to the yeast cells. Modifying the surface of

yeast presents an additional approach to enhancing biosensor electrode design, allowing for adjustments in cell–electrode contact, film conductivity, mechanical integrity, and signal reproducibility. Gold nanoparticles were integrated onto yeast cells to enhance local conductivity and promote electron exchange with redox-active sites involved in glucose-responsive mediator turnover, while polypyrrole was utilized to enhance cell immobilization stability and to form a more coherent sensing layer. A study was conducted on a combined polypyrrole–AuNP modification to assess potential synergistic effects resulting from the concurrent enhancement of biolayer stability and electronic connectivity at the sensing interface. This systematic progression from unmodified to chemically modified yeast facilitates a direct evaluation of how biolayer engineering influences the glucose-dependent electrochemical signal on AuNP-modified graphite, providing a deeper understanding of structure–function relationships pertinent to yeast-based electrochemical sensing layers.

The unmodified yeast layer on ecAu/GR (Sc/ecAu/GR) exhibited the most stable baseline behavior among the configurations containing yeast, aligning with a relatively clear mediator pathway and reduced additional barriers within the biolayer. The direct introduction of AuNPs onto yeast (Sc:Au/ecAu/GR) resulted in an increased amplitude of the glucose-driven signal. However, this did not lead to a more scalable concentration response. This indicates that while the addition of nanoparticles at the cell surface can enhance local wiring, the overall response remains limited by interfacial transport through the composite film. In contrast, the modification of PPy alone (Sc:PPy/ecAu/GR) resulted in the strongest curvature and the most rapid saturation behavior. This observation aligns with the characteristics of a denser, more resistive, and/or less permeable biolayer, which restricts the exchange of mediators and analytes at elevated substrate levels, even when the initial response is significant. The integration of PPy–AuNP yeast modification (Sc:PPy:Au/ecAu/GR) balanced these conflicting influences: it maintained the mechanical integrity anticipated from PPy while also enhancing electronic connectivity and charge transfer through the AuNP, resulting in the highest glucose-induced current increase observed among the evaluated sensing layers.

From a biosensing perspective, the glucose window investigated here (0–60 mM) was selected primarily to resolve how electrode and biolayer modifications modulate signal formation and saturation behavior in mediator-assisted yeast bioelectrodes, rather than to target an inherently linear response across the entire range. Accordingly, the calibration profiles are non-linear and approach saturation, and the response is best summarized using full-range saturating descriptors (Hill parameters) together with a defined low-glucose working calibration. Using this combined view, Sc:PPy:Au/ecAu/GR emerges as the most promising configuration within the proof-of-concept scope of the dataset, offering the most favorable balance between glucose-induced signal gain and low-range detectability among the tested sensing layers.

5. Conclusions

Electrochemical deposition of AuNPs provides a controllable route to tune the graphite–electrolyte interphase and, consequently, the mediator-assisted glucose readout of graphite-based S. cerevisiae bioelectrodes. Across the AuNP cycle series, the glucose-response profiles were non-linear and were consistently captured using Hill descriptors ($Vmax$, k, n), showing that AuNP loading affects both response curvature and signal capacity. Complementary CV, EIS, and AFM indicate that AuNP deposition increases geometric surface texture and promotes a more uniform interfacial response, while also increasing Rct—consistent with partial screening of highly active graphite microdomains for mediator exchange. When yeast-layer engineering was introduced, the combined PPy–AuNP yeast modification (Sc:PPy:Au/ecAu/GR) delivered the most favorable overall glucose-

responsive behavior among the tested architectures by balancing mechanical coherence with improved electronic/transport connectivity in the composite film. Within the proof-of-concept scope of this study, Sc:PPy:Au/ecAu/GR therefore emerges as the most promising configuration, providing the most favorable balance between glucose-induced signal gain and low-range detectability among the tested sensing layers.

Author Contributions: Conceptualization, I.M. and A.R.; methodology, T.K.-I.; software, T.K.-I., D.P., L.S. and A.Z.; validation, T.K.-I. and D.P.; formal analysis, T.K.-I.; investigation, T.K.-I.; resources; data curation, T.K.-I., D.P., L.S. and A.Z.; writing—original draft preparation, T.K.-I., D.P., L.S., A.Z., I.M. and A.R.; writing—review and editing, T.K.-I., D.P., L.S., A.Z., I.M. and A.R.; visualization, T.K.-I., D.P., L.S. and A.Z.; supervision, I.M. and A.R.; project administration funding acquisition, All authors have read and agreed to the published version of the manuscript.

Funding: This research was funded by Lithuanian Research Council, agreement number S-PD-25-14.

Institutional Review Board Statement: Not applicable.

Informed Consent Statement: Not applicable.

Data Availability Statement: The original contributions presented in this study are included in the article. Further inquiries can be directed to the corresponding author.

Conflicts of Interest: The authors declare no conflicts of interest.

Abbreviations

The following abbreviations are used in this manuscript:

MFC	Microbial Fuel Cell
AuNPs	Gold nanoparticles
PPy	Polypyrrole
PQ	9,10-phenanthrenequinone
BES	Bioelectrochemical system
Sc	*Saccharomyces cerevisiae*
AFM	atomic force microscopy
ecAu	Electrodeposited gold nanoparticles
GR	Graphite rod
CV	Cyclic voltammetry
EIS	Electrochemical impedance spectroscopy

References

1. Pullano, S.A.; Greco, M.; Bianco, M.G.; Foti, D.; Brunetti, A.; Fiorillo, A.S. Glucose biosensors in clinical practice: Principles, limits and perspectives of currently used devices. *Theranostics* **2022**, *12*, 493–511. [CrossRef] [PubMed]
2. Wu, X.; Yuan, Z.; Gao, S.; Zhang, X.; El-Mesery, H.S.; Lu, W.; Dai, X.; Xu, R. Electrochemical Biosensors Driving Model Transformation for Food Testing. *Foods* **2025**, *14*, 2669. [CrossRef]
3. Villalonga, A.; Sánchez, A.; Mayol, B.; Reviejo, J.; Villalonga, R. Electrochemical biosensors for food bioprocess monitoring. *Curr. Opin. Food Sci.* **2022**, *43*, 18–26. [CrossRef]
4. Xiao, N.; Selvaganapathy, P.R.; Wu, R.; Huang, J.J. Influence of wastewater microbial community on the performance of miniaturized microbial fuel cell biosensor. *Bioresour. Technol.* **2020**, *302*, 122777. [CrossRef] [PubMed]
5. Nawaz, A.; ul Haq, I.; Qaisar, K.; Gunes, B.; Raja, S.I.; Mohyuddin, K.; Amin, H. Microbial fuel cells: Insight into simultaneous wastewater treatment and bioelectricity generation. *Process Saf. Environ. Prot.* **2022**, *161*, 357–373. [CrossRef]
6. Yang, E.; Mohamed, H.O.; Park, S.-G.; Obaid, M.; Al-Qaradawi, S.Y.; Castaño, P.; Chon, K.; Chae, K.-J. A review on self-sustainable microbial electrolysis cells for electro-biohydrogen production via coupling with carbon-neutral renewable energy technologies. *Bioresour. Technol.* **2021**, *320*, 124363. [CrossRef]
7. Wang, Y.; Ge, L.; Wang, P.; Yan, M.; Yu, J.; Ge, S. A three-dimensional origami-based immuno-biofuel cell for self-powered, low-cost, and sensitive point-of-care testing. *Chem. Commun.* **2014**, *50*, 1947–1949. [CrossRef]
8. Fadzli, F.S.; Bhawani, S.A.; Adam Mohammad, R.E. Microbial Fuel Cell: Recent Developments in Organic Substrate Use and Bacterial Electrode Interaction. *J. Chem.* **2021**, *2021*, 4570388. [CrossRef]

9. Ucar, D.; Zhang, Y.; Angelidaki, I. An Overview of Electron Acceptors in Microbial Fuel Cells. *Front. Microbiol.* **2017**, *8*, 643. [CrossRef]
10. Jutila, E.; Koivunen, R.; Bollström, R.; Gane, P. Fully inkjet-printed glucose assay fabricated on highly porous pigment coating. *Microfluid. Nanofluid.* **2020**, *24*, 40. [CrossRef]
11. Zinovicius, A.; Rozene, J.; Merkelis, T.; Bruzaite, I.; Ramanavicius, A.; Morkvenaite-Vilkonciene, I. Evaluation of a Yeast–Polypyrrole Biocomposite Used in Microbial Fuel Cells. *Sensors* **2022**, *22*, 327. [CrossRef] [PubMed]
12. Mier, A.A.; Olvera-Vargas, H.; Mejía-López, M.; Longoria, A.; Verea, L.; Sebastian, P.; Arias, D.M. A review of recent advances in electrode materials for emerging bioelectrochemical systems: From biofilm-bearing anodes to specialized cathodes. *Chemosphere* **2021**, *283*, 131138. [CrossRef]
13. Kondrotaitė-Intė, T.; Zinovičius, A.; Pirštelis, D.; Morkvėnaitė, I. Enhancing Electron Transfer Efficiency in Microbial Fuel Cells Through Gold Nanoparticle Modification of *Saccharomyces cerevisiae*. *Microorganisms* **2025**, *13*, 1938. [CrossRef]
14. Bazina, N.; Ahmed, T.G.; Almdaaf, M.; Jibia, S.; Sarker, M. Power generation from wastewater using microbial fuel cells: A review. *J. Biotechnol.* **2023**, *374*, 17–30. [CrossRef]
15. Godain, A.; Vogel, T.M.; Fongarland, P.; Haddour, N. Influence of Hydrodynamic Forces on Electroactive Bacterial Adhesion in Microbial Fuel Cell Anodes. *Bioengineering* **2023**, *10*, 1380. [CrossRef]
16. Al-Asheh, S.; Al-Assaf, Y.; Aidan, A. Single-Chamber Microbial Fuel Cells' Behavior at Different Operational Scenarios. *Energies* **2020**, *13*, 5458. [CrossRef]
17. Zhou, M.; Chi, M.; Luo, J.; He, H.; Jin, T. An overview of electrode materials in microbial fuel cells. *J. Power Sources* **2011**, *196*, 4427–4435. [CrossRef]
18. Logan, B.E.; Hamelers, B.; Rozendal, R.; Schröder, U.; Keller, J.; Freguia, S.; Aelterman, P.; Verstraete, W.; Rabaey, K. Microbial Fuel Cells: Methodology and Technology. *Environ. Sci. Technol.* **2006**, *40*, 5181–5192. [CrossRef]
19. Kong, S.; Zhao, J.; Li, F.; Chen, T.; Wang, Z. Advances in Anode Materials for Microbial Fuel Cells. *Energy Technol.* **2022**, *10*, 2200824. [CrossRef]
20. Yaqoob, A.A.; Ibrahim, M.N.M.; Rodríguez-Couto, S. Development and modification of materials to build cost-effective anodes for microbial fuel cells (MFCs): An overview. *Biochem. Eng. J.* **2020**, *164*, 107779. [CrossRef]
21. Kižys, K.; Pirštelis, D.; Morkvėnaitė-Vilkončienė, I. Effect of Gold Nanoparticles in Microbial Fuel Cells Based on Polypyrrole-Modified *Saccharomyces cerevisiae*. *Biosensors* **2024**, *14*, 572. [CrossRef]
22. Fan, X.; Zhou, Y.; Jin, X.; Song, R.B.; Li, Z.; Zhang, Q. Carbon material-based anodes in the microbial fuel cells. *Carbon Energy* **2021**, *3*, 449–472. [CrossRef]
23. Tang, S.; Zhuang, X.; Zhao, W.; Liang, J.; Zeng, Y.; Xin, F.; Dong, W.; Jia, H.; Wu, X. Catalytic role of biogenic gold nanoparticles in improving Cr(VI) removal efficiency of biocathode microbial fuel cells. *J. Chem. Technol. Biotechnol.* **2024**, *99*, 1364–1376. [CrossRef]
24. Thapa, K.; Liu, W.; Zhang, Y.; Westenberg, D.; Zhou, Y.; Wang, R. Boosting the Power Performance of Microbial Fuel Cells by Using Dual Nanomaterial-Modified Carbon Felt Electrodes. *Energy Fuels* **2024**, *38*, 21412–21422. [CrossRef]
25. Zinovicius, A.; Morkvenaite-Vilkonciene, I.; Ramanavicius, A. Localised Electrochemical Impedance Spectroscopy of Gold Nanoparticles Labelled Antibodies Probed by Platinum Microstructured Ultramicroelectrode. *Materials* **2024**, *17*, 1339. [CrossRef] [PubMed]
26. Alalawy, A.I.; Zidan, N.S.; Sakran, M.; Hazazi, A.Y.; Salama, E.-S.; Alotaibi, M.A. Enhancing bioelectricity generation in seaweed-derived microbial fuel cells using modified anodes with Fe_2O_3@AuNPs/PANI nanocomposites. *Biomass Bioenergy* **2024**, *182*, 107104. [CrossRef]
27. Fan, Y.; Xu, S.; Schaller, R.; Jiao, J.; Chaplen, F.; Liu, H. Nanoparticle decorated anodes for enhanced current generation in microbial electrochemical cells. *Biosens. Bioelectron.* **2011**, *26*, 1908–1912. [CrossRef]
28. Wu, X.; Xiong, X.; Owens, G.; Brunetti, G.; Zhou, J.; Yong, X.; Xie, X.; Zhang, L.; Wei, P.; Jia, H. Anode modification by biogenic gold nanoparticles for the improved performance of microbial fuel cells and microbial community shift. *Bioresour. Technol.* **2018**, *270*, 11–19. [CrossRef] [PubMed]
29. Aliyah; Nasution, M.A.F.; Ayudia Putri, Y.M.; Gunlazuardi, J.; Ivandini, T.A. Modification of carbon foam with 4-mercaptobenzoic acid functionalised gold nanoparticles for an application in a yeast-based microbial fuel cell. *RSC Adv.* **2022**, *12*, 28647–28657. [CrossRef]
30. Wang, T.; Shi, P.; Wang, M.; Zhang, S. Preparation of AuNP-CQD/PDA/GO anode for MFC and its treatment of oily sewage from ships. *Environ. Sci. Pollut. Res.* **2023**, *30*, 56198–56206. [CrossRef]
31. Kus-Liśkiewicz, M.; Fickers, P.; Ben Tahar, I. Biocompatibility and Cytotoxicity of Gold Nanoparticles: Recent Advances in Methodologies and Regulations. *Int. J. Mol. Sci.* **2021**, *22*, 10952. [CrossRef]
32. Li, X. In vitro detection of nanoparticle cytotoxicity based on big data technology. *J. Comput. Methods Sci. Eng.* **2021**, *21*, 1797–1808. [CrossRef]

33. Xia, Q.; Huang, J.; Feng, Q.; Chen, X.; Liu, X.; Li, X.; Zhang, T.; Xiao, S.; Li, H.; Zhong, Z.; et al. Size- and cell type-dependent cellular uptake, cytotoxicity and in vivo distribution of gold nanoparticles. *Int. J. Nanomed.* **2019**, *14*, 6957–6970. [CrossRef] [PubMed]
34. Duman, H.; Akdaşçi, E.; Eker, F.; Bechelany, M.; Karav, S. Gold Nanoparticles: Multifunctional Properties, Synthesis, and Future Prospects. *Nanomaterials* **2024**, *14*, 1805. [CrossRef] [PubMed]
35. Saratale, R.G.; Kuppam, C.; Mudhoo, A.; Saratale, G.D.; Periyasamy, S.; Zhen, G.; Koók, L.; Bakonyi, P.; Nemestóthy, N.; Kumar, G. Bioelectrochemical systems using microalgae—A concise research update. *Chemosphere* **2017**, *177*, 35–43. [CrossRef]
36. Cheng, Y.; Ding, J.; Wan, J.; Tang, L.; Joseph, A.; Usman, M.; Zhu, N.; Zhang, Y.; Sun, H.; Rene, E.R.; et al. Improvement of biotic nitrate reduction in constructed photoautotrophic biofilm-soil microbial fuel cells. *J. Environ. Manag.* **2024**, *360*, 121066. [CrossRef]
37. Dai, M.; Wu, Y.; Wang, J.; Lv, Z.; Li, F.; Zhang, Y.; Kong, Q. Constructed wetland-microbial fuel cells enhanced with iron carbon fillers for ciprofloxacin wastewater treatment and power generation. *Chemosphere* **2022**, *305*, 135377. [CrossRef]
38. Singh, A.; Kaushik, A. Removal of Cd and Ni with enhanced energy generation using biocathode microbial fuel cell: Insights from molecular characterization of biofilm communities. *J. Clean. Prod.* **2021**, *315*, 127940. [CrossRef]
39. Geetanjali; Rani, R.; Kumar, S. Microbial community dynamics of microbial fuel cell in response to NiWO4/rGO nanocomposites as electrocatalyst and its correlation with electrochemical properties. *J. Environ. Chem. Eng.* **2021**, *9*, 104668. [CrossRef]
40. Wang, H.; Long, X.; Cao, X.; Li, L.; Zhang, J.; Zhao, Y.; Wang, D.; Wang, Z.; Meng, H.; Dong, W.; et al. Stimulation of atrazine degradation by activated carbon and cathodic effect in soil microbial fuel cell. *Chemosphere* **2023**, *320*, 138087. [CrossRef]
41. Samudro, G.; Imai, T.; Hung, Y.-T. Enhancement of Power Generation and Organic Removal in Double Anode Chamber Designed Dual-Chamber Microbial Fuel Cell (DAC-DCMFC). *Water* **2021**, *13*, 2941. [CrossRef]
42. Kuo, J.; Liu, D.; Lin, C.-H. Functional Prediction of Microbial Communities in Sediment Microbial Fuel Cells. *Bioengineering* **2023**, *10*, 199. [CrossRef] [PubMed]
43. Verma, M.; Mishra, V. Recent trends in upgrading the performance of yeast as electrode biocatalyst in microbial fuel cells. *Chemosphere* **2021**, *284*, 131383. [CrossRef]
44. Rozene, J.; Morkvenaite-Vilkonciene, I.; Bruzaite, I.; Dzedzickis, A.; Ramanavicius, A. Yeast-based microbial biofuel cell mediated by 9,10-phenantrenequinone. *Electrochim. Acta* **2021**, *373*, 137918. [CrossRef]
45. Rozene, J.; Morkvenaite-Vilkonciene, I.; Bruzaite, I.; Zinovicius, A.; Ramanavicius, A. Baker's Yeast-Based Microbial Fuel Cell Mediated by 2-Methyl-1,4-Naphthoquinone. *Membranes* **2021**, *11*, 182. [CrossRef]
46. Arun, S.; Sinharoy, A.; Pakshirajan, K.; Lens, P.N. Algae based microbial fuel cells for wastewater treatment and recovery of value-added products. *Renew. Sustain. Energy Rev.* **2020**, *132*, 110041. [CrossRef]
47. Kaneshiro, H.; Takano, K.; Takada, Y.; Wakisaka, T.; Tachibana, T.; Azuma, M. A milliliter-scale yeast-based fuel cell with high performance. *Biochem. Eng. J.* **2014**, *83*, 90–96. [CrossRef]
48. Haslett, N.D.; Rawson, F.J.; Barrière, F.; Kunze, G.; Pasco, N.; Gooneratne, R.; Baronian, K.H. Characterisation of yeast microbial fuel cell with the yeast Arxula adeninivorans as the biocatalyst. *Biosens. Bioelectron.* **2011**, *26*, 3742–3747. [CrossRef]
49. Sekrecka-Belniak, A.; Toczyłowska-Maminska, R. Fungi-Based Microbial Fuel Cells. *Energies* **2018**, *11*, 2827. [CrossRef]
50. Gao, G.; Fang, D.; Yu, Y.; Wu, L.; Wang, Y.; Zhi, J. A double-mediator based whole cell electrochemical biosensor for acute biotoxicity assessment of wastewater. *Talanta* **2017**, *167*, 208–216. [CrossRef] [PubMed]
51. Rawson, F.J.; Downard, A.J.; Baronian, K.H. Electrochemical detection of intracellular and cell membrane redox systems in Saccharomyces cerevisiae. *Sci. Rep.* **2014**, *4*, 5216. [CrossRef]
52. Bocina, E.; Cocuzza, C.; Vincenzi, C.; Fino, D.; Cauda, V.; Piumetti, M. Enzyme-based biosensors: Emerging tools for advanced biomedical applications. *Talanta* **2026**, *300*, 129241. [CrossRef]
53. Guoqiang, G.; Liang, Q.; Yani, Z.; Pengyun, W.; Fanzhuo, K.; Yuyang, Z.; Zhiyuan, L.; Xing, N.; Xue, Z.; Qiongya, L.; et al. Recent advances in glucose monitoring utilizing oxidase electrochemical biosensors integrating carbon-based nanomaterials and smart enzyme design. *Front. Chem.* **2025**, *13*, 1591302. [CrossRef]
54. Moraskie, M.; Roshid, M.H.; O'Connor, G.; Dikici, E.; Zingg, J.-M.; Deo, S.; Daunert, S. Microbial whole-cell biosensors: Current applications, challenges, and future perspectives. *Biosens. Bioelectron.* **2021**, *191*, 113359. [CrossRef]
55. Gui, Q.; Lawson, T.; Shan, S.; Yan, L.; Liu, Y. The Application of Whole Cell-Based Biosensors for Use in Environmental Analysis and in Medical Diagnostics. *Sensors* **2017**, *17*, 1623. [CrossRef] [PubMed]
56. Andriukonis, E.; Stirkė, A.; Mikoliunaite, L.; Balevicius, Z.; Ramanavičiene, A.; Ramanavičius, A. Pyrrole Bio-Polymerization Using Redox Mediator. Patent No. LT6239B, 11 January 2016.
57. German, N.; Ramanavicius, A.; Ramanaviciene, A. Amperometric Glucose Biosensor Based on Electrochemically Deposited Gold Nanoparticles Covered by Polypyrrole. *Electroanalysis* **2017**, *29*, 1267–1277. [CrossRef]
58. Lu, C.; Xu, J.; Song, Z.; Zhu, G.; Dai, Z. A novel multifunctional fluorescent probe with ESIPT and AIE effects for the detection of Co^{2+} and HClO. *RSC Adv.* **2025**, *15*, 4000–4013. [CrossRef] [PubMed]
59. Nigam, R.; Kar, K.K. Simulation Study of Electric Double-Layer Capacitance of Ordered Carbon Electrodes. *Langmuir* **2022**, *38*, 12235–12247. [CrossRef]

60. Ko, Y.; Kwon, C.H.; Lee, S.W.; Cho, J. Nanoparticle-Based Electrodes with High Charge Transfer Efficiency through Ligand Exchange Layer-by-Layer Assembly. *Adv. Mater.* **2020**, *32*, e2001924. [CrossRef]
61. Yin, X.-T.; You, E.-M.; Zhou, R.-Y.; Zhu, L.-H.; Wang, W.-W.; Li, K.-X.; Wu, D.-Y.; Gu, Y.; Li, J.-F.; Mao, B.-W.; et al. Unraveling the energy storage mechanism in graphene-based nonaqueous electrochemical capacitors by gap-enhanced Raman spectroscopy. *Nat. Commun.* **2024**, *15*, 5624. [CrossRef]
62. Lehane, R.A.; Gamero-Quijano, A.; Manzanares, J.A.; Scanlon, M.D. Mechanistic Insights into the Potentiodynamic Electrosynthesis of PEDOT Thin Films at a Polarizable Liquid | Liquid Interface. *J. Am. Chem. Soc.* **2024**, *146*, 28941–28951. [CrossRef]
63. Aziz, S.B.; Brza, M.A.; Dannoun, E.M.A.; Hamsan, M.H.; Hadi, J.M.; Kadir, M.F.Z.; Abdulwahid, R.T. The Study of Electrical and Electrochemical Properties of Magnesium Ion Conducting CS: PVA Based Polymer Blend Electrolytes: Role of Lattice Energy of Magnesium Salts on EDLC Performance. *Molecules* **2020**, *25*, 4503. [CrossRef] [PubMed]
64. Lazanas, A.C.; Prodromidis, M.I. Electrochemical Impedance Spectroscopy—A Tutorial. *ACS Meas. Sci. Au* **2023**, *3*, 162–193. [CrossRef] [PubMed]
65. Di Giulio, T.; Mazzotta, E.; Malitesta, C. Molecularly Imprinted Polyscopoletin for the Electrochemical Detection of the Chronic Disease Marker Lysozyme. *Biosensors* **2021**, *11*, 3. [CrossRef] [PubMed]
66. Kim, Y.-E.; Jo, H.; Kwon, J.; Kim, S.-G.; Jung, C. Comparative Study of Degradation Mechanisms of Commercial Supercapacitors at High Temperatures Depending on Storage Conditions. *J. Electrochem. Soc.* **2022**, *169*, 120530. [CrossRef]
67. Kim, Y.-J.; Chinnadayyala, S.R.; Le, H.T.N.; Cho, S. Sensitive Electrochemical Non-Enzymatic Detection of Glucose Based on Wireless Data Transmission. *Sensors* **2022**, *22*, 2787. [CrossRef]
68. Dey, N.; Samuel, G.V.; Raj, D.S.; Gajalakshmi, B. Nanomaterials as Potential High Performing Electrode Materials for Microbial Fuel Cells. *Appl. Nanosci.* **2023**, *13*, 2625–2640. [CrossRef]
69. Wu, X.; Li, X.; Shi, Z.; Wang, X.; Wang, Z.; Li, C.M. Electrospinning Mo-Doped Carbon Nanofibers as an Anode to Simultaneously Boost Bioelectrocatalysis and Extracellular Electron Transfer in Microbial Fuel Cells. *Materials* **2023**, *16*, 2479. [CrossRef]
70. Li, L.; He, X.; Li, H.; Lu, Y.; Song, H.; Cheng, S. Enhancing Performance of Microbial Fuel Cell by Binder-Free Modification of Anode with Reduced Graphene Oxide through One-Step Electrochemical Exfoliation and In Situ Electrodeposition. *ACS Appl. Bio Mater.* **2025**, *8*, 642–651. [CrossRef]
71. Liu, Y.; Zhang, X.; Zhang, Q.; Li, C. Microbial Fuel Cells: Nanomaterials Based on Anode and Their Application. *Energy Technol.* **2020**, *8*, 2000206. [CrossRef]
72. Hirsch, L.O.; Gandu, B.; Chiliveru, A.; Amar Dubrovin, I.; Rozenfeld, S.; Schechter, A.; Cahan, R. The Performance of a Modified Anode Using a Combination of Kaolin and Graphite Nanoparticles in Microbial Fuel Cells. *Microorganisms* **2024**, *12*, 604. [CrossRef] [PubMed]

Disclaimer/Publisher's Note: The statements, opinions and data contained in all publications are solely those of the individual author(s) and contributor(s) and not of MDPI and/or the editor(s). MDPI and/or the editor(s) disclaim responsibility for any injury to people or property resulting from any ideas, methods, instructions or products referred to in the content.